AGU PUBLICATIONS

Journal of Advances in Modeling Earth Systems

RESEARCH ARTICLE
10.1002/2017MS000927

Key Points:
- A diagnostic sublayer parameterization scheme for SST diurnal cycle was incorporated into the global NEMO
- Three different sublayer temperature profiles (constant, linear, and exponential) for SST diurnal cycle sublayer scheme were evaluated
- The exponential sublayer temperature profile shows the most reasonable diurnal warming simulation results

Supporting Information:
- Supporting Information S1

Correspondence to:
Z. Song,
songroy@fio.org.cn

Citation:
Yang, X., Z. Song, Y.-H. Tseng, F. Qiao, and Q. Shu (2017), Evaluation of three temperature profiles of a sublayer scheme to simulate SST diurnal cycle in a global ocean general circulation model, *J. Adv. Model. Earth Syst.*, *9*, doi:10.1002/2017MS000927.

Received 24 JAN 2017
Accepted 1 AUG 2017
Accepted article online 5 AUG 2017

Evaluation of three temperature profiles of a sublayer scheme to simulate SST diurnal cycle in a global ocean general circulation model

Xiaodan Yang[1,2,3], Zhenya Song[2,3], Yu-Heng Tseng[4,5], Fangli Qiao[2,3,6], and Qi Shu[2,3]

[1]College of Oceanic and Atmospheric Sciences, Ocean University of China, Qingdao, China, [2]Laboratory for Regional Oceanography and Numerical Modeling, Qingdao National Laboratory for Marine Science and Technology, Qingdao, China, [3]Division of Marine Science and Numerical Modeling, First Institute of Oceanography, State Oceanic Administration, Qingdao, China, [4]Climate and Global Dynamics Laboratory, National Center for Atmospheric Research, Boulder, USA, [5]Now at Department of Atmospheric Sciences, National Taiwan University, [6]Key Laboratory of Marine Science and Numerical Modeling, State Oceanic Administration, Qingdao, China

Abstract The diurnal cycle of sea surface temperature (SST) plays an important role in the upper ocean and climate system. One way to represents the diurnal variation of SST in Ocean General Circulation Models (OGCMs) with coarse vertical resolution is to parameterize the diurnal cycle of SST without considering detailed dynamic processes within the mixed layer. In this study, a diagnostic sublayer parameterization scheme following Schiller and Godfrey (2005) was incorporated into a global OGCM (NEMO), for the first time, to simulate the diurnal cycle of SST. Moreover, three different sublayer temperature profiles (constant, linear, and exponential) were evaluated. Comparison with satellite SST and mooring temperature data indicated that the parameterization scheme with an exponential temperature profile showed the most reasonable diurnal warming simulation results, significantly improving the probability of (from 1.7% with constant temperature profile to 13.4%) diurnal SST amplitude larger than 1.0°C. Furthermore, the mean biases in each season were all reduced to less than 0.16°C, in good agreement with observations.

1. Introduction

The critical role of the sea surface temperature (SST) diurnal cycle, which is one of the most dominant features in SST, is recently attracting more and more attention in climate models. Previous studies have shown that the negative bias in tropical cold tongue areas can be reduced by up to 1°C after incorporating the SST diurnal cycle into a coupled model [*Bernie et al.*, 2008; *Danabasoglu et al.*, 2006]. Moreover, it impacts the climate system at different time scales, such as the Madden-Julian oscillation (MJO) at the intraseasonal time scale [*Bernie et al.*, 2008] and the El Niño-Southern Oscillation (ENSO) at the interannual time scale [*Danabasoglu et al.*, 2006; *Ham et al.*, 2010; *Masson et al.*, 2012].

To simulate the diurnal cycle of SST in an ocean general circulation model (OGCM), accurate diurnally varying atmospheric forcing (especially the shortwave radiation, SWR) is a prerequisite. Better representation of the diurnal warm layer in an OGCM is also important. The diurnal warm layer occurs when temperature stratification near the surface is strong due to the absorption of the SWR during the day. Two methods can be used to reproduce the diurnal warm layer in the ocean model. One is to directly simulate it by increasing vertical resolution of an OGCM [*Bernie et al.*, 2008; *Masson et al.*, 2012]. Based on a one-dimensional ocean model, *Bernie et al.* [2005] suggested that using high resolution in the atmospheric forcing in both time (O(3 hourly)) and space near the sea surface (O(1 m)) could capture 90% of the diurnal amplitude of SST (hereafter dSST). *Bernie et al.* [2008] and *Masson et al.* [2012] further proved that the vertical resolution of 1 m in the upper 100 m is a necessary condition to simulate the diurnal warm layer and the diurnal variation of SST successfully. However, such a high ocean-model vertical resolution within the coupled global circulation model is still a challenge. In the Coupled Model Intercomparison Project Phase 5 (CMIP5), the top layers' thicknesses are approximately 10 m in more than half (64%, 32 out of 50) ocean-model components [*Flato et al.*, 2013], which is unable to capture the reasonable diurnal variation [*Bernie et al.*, 2005]. Moreover, in the upcoming CMIP6, at least 20 climate models still use *z* coordinate model with top level thickness larger

than 5 m in their ocean-model components, suggesting increasing the vertical resolution is not practical at this moment (https://github.com/WCRP-CMIP/CMIP6_CVs/blob/master/CMIP6_source_id.json). The other viable approach is to include a sublayer parameterization in the OGCM while keeping the existing vertical resolution, which has been shown to simulate diurnal variation effectively without increasing vertical resolution [*Large and Caron*, 2015; *Schiller and Godfrey*, 2005*; Zeng and Beljaars*, 2005].

In 2005, two sublayer parameterization schemes were proposed to estimate the diurnal cycle in the ocean model. One was proposed by *Zeng and Beljaars* [2005] (referred to as the ZB05 scheme), which is a prognostic approach that assumes the sublayer depth to be constant and that temperature decreases with depth in the sublayer. The other was proposed by *Schiller and Godfrey* [2005] (referred to as the SG05 scheme), which is a diagnostic approach that estimates the sublayer depth using bulk Richardson number and assumes the temperature in the sublayer is independent of depth. *Filipiak et al*. [2012] evaluated the performance of the ZB05 scheme for diurnal warming, and found that less warming occurred at low wind speeds and larger warming occurred at moderate wind speeds. As the sublayer depth is fixed at a constant (3 m) in the ZB05 scheme, the sublayer depth in reality shallower than it simulated by the ZB05 scheme when the wind speed was low. And under the high wind speed, the observed sublayer depth could be much deeper than the modeled one. Moreover, the vertical temperature profiles from in-situ measurements also showed suggested that sublayer depth changes in accordance with the weather conditions [*Webster et al*., 1996; *Soloviev and Lukas*, 1997; *Gentemann et al*., 2009]. Thus, the varying sublayer depth in the SG05 scheme due to different weather conditions, although it is a diagnostic scheme, seems to be more reasonable. Recently, *Large and Caron* [2015] tested an OGCM with diurnal variation based on the ZB05 scheme, the first attempt to include a sublayer scheme into a global OGCM. However, they only examined the annual mean dSST without further evaluation of dSST at seasonal or intraseasonal time scale, which directly affect seasonal heat fluxes and the simulation of MJO. Until now, the performance of the SG05 scheme has not yet been examined on a global scale.

In the SG05 scheme, the sublayer temperature profile should be given in advance, which caused some disagreements in previous studies. As mentioned above, the proposed temperature profile in the original SG05 scheme is homogenous. *Fairall et al*. [1996] suggested that the water temperature should be assumed to decrease linearly from surface to bottom in a warm-layer model, which was proposed to correct in situ water temperatures for diurnal warming effect and was similar to the SG05 scheme in general. However, *Gentemann et al*. [2009] suggested that the diurnal warming in *Fairall et al*. [1996] was underestimated, and proposed a temperature profile that decreases exponentially in the warm-layer with attenuation coefficient related to wind speed. As pointed out in *Schiller and Godfrey* [2005], the uniform sublayer temperature might be problematic in simulating the diurnal cycle of SST if a strong thermal stratification exists near the surface. Thus, it is necessary to examine the capability of diurnal cycle simulation with different temperature profiles in the sublayer scheme to select the best diurnal simulation for global OGCM.

In this study, we not only incorporate the SG05 scheme into the Nucleus for European Modelling of the Ocean (NEMO) model at the global scale but also investigate detailed impacts of the diurnal parameterization at different time scales. Two additional temperature profiles of linear and exponential following *Fairall et al*. [1996] and *Gentemann et al*. [2009], respectively, are also applied to the SG05 scheme, and evaluated. The paper is organized as follows. Descriptions of the sublayer parameterization scheme with three temperature profiles and the NEMO model are provided in section 2. Sublayer depth and diurnal warming from the model results are evaluated in section 3. Conclusions and an outlook for our future work are given in section 4.

2. Methodology

2.1. Observational Data

2.1.1. AMSR-E Satellite Data

The Advanced Microwave Scanning Radiometer-Earth Observing System (AMSR-E) is on board the Aqua satellite, which was launched in May 2002. The polar orbit yields a coverage from 89.5°N to 89.5°S with a spatial resolution of 0.25°. As the local overpass times of the AMSR-E, satellite data are fixed at about 1:30 A.M./P.M. each day, and the difference between daytime and nighttime SSTs can approximately be regarded as dSST. The nighttime SST on the same day of the daytime SST is used to capture the true diurnal warming during

the daytime. dSST from the model is calculated using the SSTs at the same times (day and night) of the satellite data.

2.1.2. IMET Mooring Data

In this study, we also used the data from the Improved Meteorological Instrument (IMET) on the Woods Hole Oceanographic Institution (WHOI) mooring located at 156°E, 1°45S in the western Pacific during the Tropical Ocean Global Atmosphere/Coupled Ocean Atmosphere Response Experiment (TOGA/COARE). The resolution of the mooring data is about 1 h with 10 layers in the top 10 m, which can capture the diurnal cycle in skin SST and temperature profiles in the subsurface. Moreover, the measurements have been used in analyzing the intraseasonal variation of SST in response to the MJO [*Bernie et al*., 2005, 2007]. The sublayer depth and SST from the model at model grid points are linearly interpolated to the mooring location.

2.2. Sublayer Parameterization Scheme and Temperature Profiles

The sublayer parameterization scheme incorporated into the top model layer in this study is based on the SG05 scheme. After the solar radiation exceeds the heat loss at the surface, a sublayer will be formed near the surface, and both heat and momentum fluxes will be confined above the sublayer depth D_T. D_T is estimated by using the bulk Richardson number lower than a threshold value, which is set to 0.65 as in *Fairall et al*. [1996] and *Schiller and Godfrey* [2005]. To find the most appropriate temperature profile in the sublayer, we designed three experiments with different temperature profiles in the sublayer parameterization scheme in this study (Figure 1): EXP_SG05 (constant temperature profile), EXP_F96 (linear temperature profile), and EXP_G09 (exponential temperature profile).

2.2.1. Sublayer Depth

Here, we briefly describe the sublayer depth used in these experiments. First, the constant temperature profile in EXP_SG05 is defined the same way as that in the SG05 scheme. The sublayer depth D_T is estimated as follows:

$$D_T = \left(\frac{\rho c_p Ri_c I_\tau}{\alpha g I_s}\right)^{1/2}, \tag{1}$$

where D_T is sublayer depth, ρ is seawater density, c_p is the volumetric heat capacity, Ri_c is bulk Richardson number, I_τ is the integral of momentum flux, I_s is the integral of heat flux, α is the thermal expansion coefficient, and g is the gravity acceleration.

Second, the sublayer temperature profile in EXP_F96 is linear [*Fairall et al*., 1996], so the equation used to estimate D_T becomes:

$$D_T = \left(\frac{2\rho c_p Ri_c I_\tau}{\alpha g I_s}\right)^{1/2}, \tag{2}$$

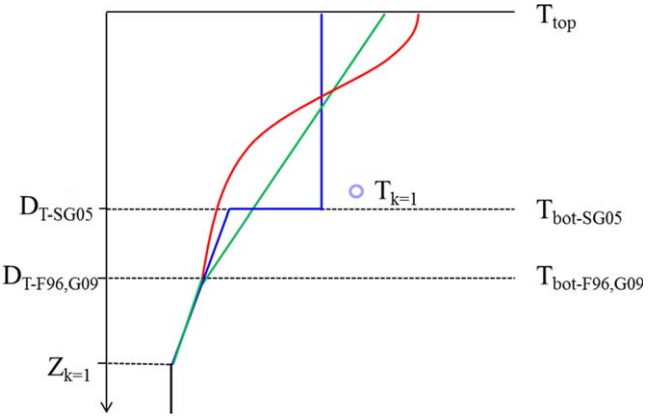

Figure 1. Schematic of vertical temperature profiles above the sublayer depth in EXP_SG05 (blue), EXP_F96 (green), and EXP_G09 (red). DT-SG05 denotes the sublayer depth used in EXP_SG05. DT-F96, G09 represents the sublayer depth used in EXP_F96 and EXP_G09. Zk = 1 represents the depth of the top model layer. Tk = 1 is the temperature of the top model layer. Ttop is the temperature at the top of the sublayer, which is also the SST in the model, and Tbot is the temperature at the bottom of the sublayer.

Following *Gentemann et al*. [2009], the sublayer depth in EXP_G09 is defined the same way as that in EXP_F96.

Note that if the calculated sublayer depth is larger than the model's top layer depth (10 m here), we assume the sublayer is not formed.

2.2.2. Diurnal Warming

If the sublayer is not present, the change of SST is equal to the variation of the temperature in the top layer of the model ($\triangle T_{k=1}$ for each time step). If the sublayer is formed, the variation of SST in EXP_SG05 is equal to the change of the temperature at the top of the sublayer, which is given by the formula below (similar to *Schiller and Godfrey*, [2005]):

$$\Delta T_{top}(t)=\Delta T_{k=1}(t)+\frac{I_{sw}(t)}{\rho C_p}\left(\frac{1-f_w(-D_T(t))}{D_T(t)}-\frac{1-f_w(-z_{k=1})}{z_{k=1}}\right)-\frac{I_{surf}(t)}{\rho C_p}\left(\frac{1}{D_T(t)}-\frac{1}{z_{k=1}}\right) \quad (3)$$

where $z_{k=1}$ represents the depth of the top model layer. f_w is the penetration of the SWR into the ocean.

In EXP_F96, the change of the temperature at the top of the sublayer $\Delta T_{top}(t)$ becomes:

$$\Delta T_{top}(t)=\Delta T_{k=1}(t)+\frac{I_{sw}(t)}{\rho c_p}\left(2\frac{1-f_w(-D_T(t))}{D_T(t)}+\partial f_w(z)/\partial z-\frac{1-f_w(-z_{k=1})}{z_{k=1}}\right)-\frac{I_{surf}(t)}{\rho c_p}\left(\frac{2}{D_T(t)}-\frac{1}{z_{k=1}}\right) \quad (4)$$

where $\frac{I_{sw}(t)}{\rho c_p}\frac{\partial f_w(z)}{\partial z}$ represents the variation of temperature at the bottom of the sublayer due to the SWR penetration.

For EXP_G09, the temperature profile in the sublayer following *Gentemann et al*. [2009] is:

$$\Delta T(z)=(T_{top}-T_{bot})e^{-9.5\left(\frac{z}{D_T}\right)^a}, \quad (5)$$

where a is a coefficient related to wind speed. $\Delta T_{top}(t)$ in EXP_G09 can be estimated as follows:

$$\Delta T_{top}(t)=\Delta T_{k=1}(t)+\frac{I_{sw}(t)}{\rho c_p}\left(S\frac{(1-f_w(-D_T(t)))}{D_T(t)}+\partial f_w(z)/\partial z-\frac{1-f_w(-z_{k=1})}{z_{k=1}}\right)-\frac{I_{surf}(t)}{\rho c_p}\left(\frac{s}{D_T(t)}-\frac{1}{z_{k=1}}\right) \quad (6)$$

where $S=D_T/\int_0^{D_T}e^{-9.5\left(\frac{z}{D_T}\right)^a}dz$. The details of the derivation are given in supporting information Appendix A. It should be noted that the effect of cool skin temperature is not considered in this study to be consistent with the SG05 scheme. Since the cool skin effect occurs in both daytime and nighttime, it will not greatly influence dSST which is our main focus of this study.

2.3. Ocean General Circulation Model

The OGCM used in this study is the NEMO model version 3.4 [*Madec*, 2008]. The configuration is called ORCA2, which has a tripolar horizontal curvilinear mesh with a nominal resolution of 2°. There are 31 vertical layers. The resolution is 10 m in the upper 100 m and increases gradually to 500 m at depth.

The initial conditions of temperature and salinity are from the combination of the World Ocean Atlas 2009 [*Antonov et al*., 2010; *Locarnini et al*., 2010] and the Polar Science Center Hydrographic Climatology version 3 (updated from *Steele et al*. [2001]) data. The daily-mean SWR is reconstructed to a 3 hourly resolution (i.e., explicit diurnal cycle) using the method proposed in *Bernie et al*. [2007]. The SWR penetration is computed based on two-band absorption profiles for Jerlov water-type I [*Jerlov*, 1976].

$$f_w(z)=0.58\times e^{(-z/0.35)}+0.42\times e^{(-z/23.)} \quad (7)$$

The atmospheric forcing is the interannually (1948–2009) varying CORE2 forcing data set [*Griffies et al*., 2009; *Large and Yeager*, 2009]. The CORE bulk formulae developed by *Large and Yeager* [2004] is used to compute sensible and latent heat fluxes. In this study, the top layer temperature, namely, SST, is replaced with the temperature at the top of the sublayer when a sublayer is present. Since the sublayer scheme has not been verified in sea-ice areas, it is only incorporated into ice-free ocean. The experiments were spun up for 124 years (two cycles of CORE2 forcing). The model outputs used for analyses are from 2002 to 2009 of the second cycle, to compare with the AMSR-E SST during June 2002 to December 2009.

3. Results

3.1. Sublayer Depth

The 8 year (from 2002 to 2009) averages of sublayer depth, peak SWR, and wind speed are shown in Figure 2. Note that when the sublayer is not formed, the sublayer depth is set to the top model layer depth, which is 10 m in this study, to calculate the averaged sublayer depth. Shallow sublayer mainly occurs in the tropical areas. It is more consistent with the distribution of wind speed than with the peak SWR since the correlation coefficient between sublayer depth and wind speed could reach 0.85, while the correlation coefficient between sublayer depth and peak SWR is only −0.10. As explained by *Clayson and Weitlich* [2007], the variation of peak SWR in the tropic is less than 200 W/m^2 in the range of 550–750 W/m^2, while the mean change

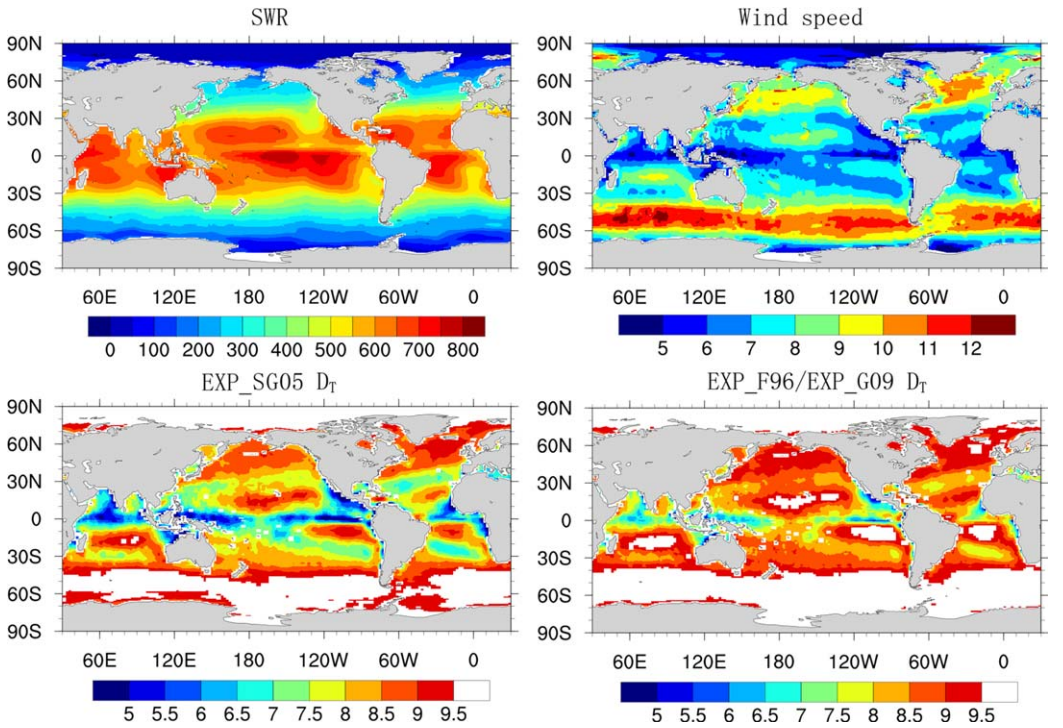

Figure 2. Climatological distributions of the peaks of (top left) SWR and (top right) wind speed, and of sublayer depth in (bottom left) EXP_SG05 and (bottom right) EXP_F96/EXP_G09 during June 2002 to December 2009. The time of the sublayer analysis is the same as the AMSR-E satellite local overpass time, which is approximately 1:30 P.M.

in wind speed is relatively large from 3 to 9 m/s, which is responsible for the large variance of sublayer depth spatially.

According to equations (1) and (2), the mean sublayer depth is shallower in EXP_SG05 (less than 5 m) than in EXP_F96/EXP_G09 (around 5–7 m) in the Arabian Sea, the western Pacific warm pool, the eastern Pacific cold tongue area, the west coast off California, and the west coast of Africa, when the mean wind speed is less than 5 m/s (Figure 2). The mean sublayer depth is deeper than 8 m in EXP_SG05 and approximately 10 m in EXP_F96/EXP_G09 when the mean wind speed larger than 7 m/s. This suggests that sublayers are rarely formed in the northern central Pacific, northwest off South America, southern central Indian Ocean, and southern central Atlantic. In the westerlies region, the sublayer is not established in these experiments due to strong wind.

3.2. Diurnal Warming

3.2.1. Annual Mean

Before examining diurnal warming in model sensitivity of the sublayer parameterization, we first evaluate the dSST calculated using temperatures in the top model layer (figure not shown here). The results indicate that 99.7% of the dSST is less than 0.3°C and the rest is between 0.3 and 0.5°C, similar to the modeled peak dSST of 0.28°C in *Danabasoglu et al*. [2006]. However, the dSST in the observations under favorable conditions could reach 2–3°C or more [*Kawai and Wada* 2007]. As illustrated in *Bernie et al*. [2008], a 10 m vertical resolution could only capture 20.0% of the dSST due to the distribution of heat fluxes in the thick layer. In this study, the NEMO model with 10 m vertical resolution cannot simulate accurate dSST.

Figure 3 shows dSST as a function of wind speed and peak SWR in AMSR-E data and model results. We can see that weaker wind speed and larger peak SWR lead to higher probability of large diurnal warming. In the AMSR-E data, when the wind speed is less than 3 m/s, dSST has a high probability of being larger than 1°C; when the wind speed is less than 2 m/s and peak SWR is larger than 400 W/m^2, dSST could be larger than 2°C. The total percentage of dSST larger than 3°C is 0.8%, of dSST being 2–3°C is 2.7% and of dSST being 1–2°C is 15.9% in the AMSR-E data (Table 1).

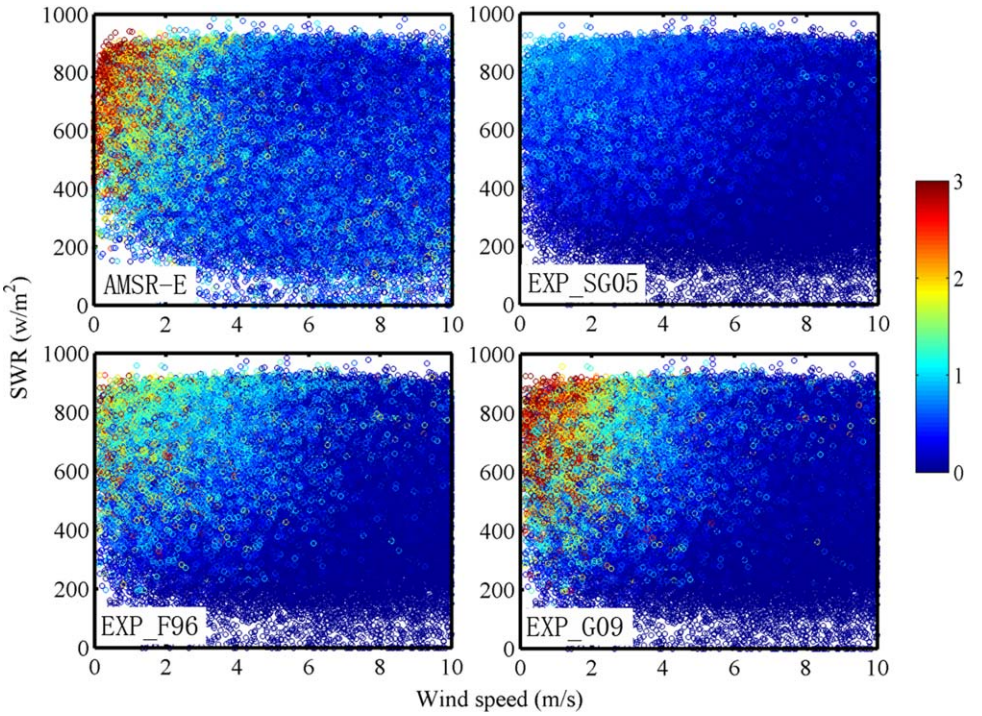

Figure 3. dSST as a function of wind speed and peak SWR from (top left) AMSR-E satellite data, and (top right) from EXP_SG05, (bottom left) EXP_F96, and (bottom right) EXP_G09.

Different from the satellite data, a dSST larger than 2°C does not occur in EXP_SG05, and the percentage of dSST larger than 1°C is only 1.0% in EXP_SG05. This may be due to the homogenous temperature profile used in the sublayer under all weather conditions. When the wind speed is small and peak SWR is large, the stratification in the sublayer should be strong instead of a uniform sublayer. Thus, large diurnal warming could be underestimated in EXP_SG05. As the wind speed becomes strong and peak SWR becomes weak, 63.3% of dSST drops to less than 0.3°C, of which 40.2% is due to the absence of sublayer while another 23.1% could be caused by the underestimation of the sublayer scheme.

In EXP_F96, the probability of dSST larger than 3°C is about 0.3%, and that between 2 and 3°C is 0.9%; it mainly occurs at wind speeds less than 2 m/s. The probability is larger than that in EXP_SG05 but still much less than that of the observations. The probability of dSST between 1 and 2°C increases from 1.0% in EXP_SG05 to 10.3% in EXP_F96, closer to the observations. Moreover, the probability of dSST below 0.3°C decreases from 63.3% in EXP_SG05 to 59.0% in EXP_F96, of which 53.5% is due to the absence of sublayer. As discussed in supporting information Appendix A, there is more probability of the sublayer not being formed in EXP_F96 than in EXP_SG05, but when the sublayer could be formed, the probability of dSST less than 0.3°C decreases from 23.1% in EXP_SG05 to 5.5% in EXP_F96.

In EXP_G09, dSST larger than 3°C occurs when the wind speed is less than 2 m/s and peak SWR is larger than 400 W/m^2. The associated probability reaches 1.3%, slightly larger than that of the AMSR-E data (0.8%). However, the largest dSST in EXP_G09 could be more than 10.0°C, while the largest dSST in AMSR-E is no more than 9.5°C. The overestimate of dSST was previously noted by *Filipiak et al.* [2012] and *Weihs and Bourassa* [2014]. The overestimation can be partially explained by the heat conduction and momentum dissipation at the base of the sublayer, which were considered in *Gentemann et al.* [2009] but ignored in EXP_G09 to be consistent with the SG05 scheme. Moreover, the Jerlov water-type used may also lead to some degree of overestimations (see the discussion in section 4).The

Table 1. Probability (%) of dSST in the AMSR-E Data and in EXP_SG05, EXP_F96 and EXP_G09

	0–0.3	0.3–0.5	0.5–1	1–2	2–3	>3
AMSR-E	27.7	20.2	32.7	15.9	2.7	0.8
EXP_SG05	63.3	19.9	15.9	1.0	0.0	0.0
EXP_F96	59.0	7.6	22.0	10.3	0.9	0.3
EXP_G09	61.0	9.1	16.6	9.6	2.5	1.3

probability of dSST between 2 and 3°C is 2.5%, and that between 1 and 2°C is 9.6%, which are in good agreement with the satellite data results.

The comparison of the three sensitivity experiments suggests the sublayer parameterization in EXP_G09 is much better in terms of simulating large diurnal warming than in other experiments. One of the reasons may be that the exponential temperature profile in EXP_G09 was proposed based on in situ temperature observations with high vertical resolution [*Gentemann et al*., 2009]. Another reason may be that the exponential distribution of temperature matches well with the distribution of SWR in the upper ocean. According to equation (7), the profile of absorption of SWR is supposed to be exponential, contributing to the upper ocean temperature distribution under low wind speed. As the wind speed increases, the mixing near the surface increases with weaker temperature gradient in the upper ocean, which is also shown in the temperature profile in EXP_G09 using attenuation coefficients related to wind speed.

The results show that the probability of the dSST less than 0.3°C, which is mainly caused by the absence of a sublayer, could be more than 55.0% in each of the three experiments, larger than the probability of 27.7% in the AMSR-E data. As discussed above, the sublayer cannot be formed when its depth is larger than the top model layer thickness, which is 10 m in this study. In *Fairall et al*. [1996] and *Gentemann et al*. [2009], the maximum warm-layer thickness was set to 19 m, leading to an increased probability of the warm-layer being formed. Thus, the much larger probability of dSST less than 0.3°C may be due to the rigorous criteria for the sublayer to be formed, which needs to be improved in future research.

The modeled global distributions of annual-mean dSST are compared with the AMSR-E satellite results in Figure 4, which illustrates similar large-scale patterns in general. The large dSST of more than 0.5°C in the satellite data is located mainly in the tropics, such as the eastern Pacific cold tongue area, the western Pacific warm pool, the northern Indian Ocean, and the west coast off California, which agrees well with the areas of weak winds (Figure 2). In the areas across the North Pacific, the northern central Atlantic and between 20°S–30°S in the Southern Hemisphere, the annual-mean dSST is between 0.2 and 0.4°C with moderate wind speeds. Other areas with small dSST of less than 0.2°C correspond to large wind speeds, such as the northern central Pacific, off northwest South America, southern central Indian Ocean, and southern central Atlantic.

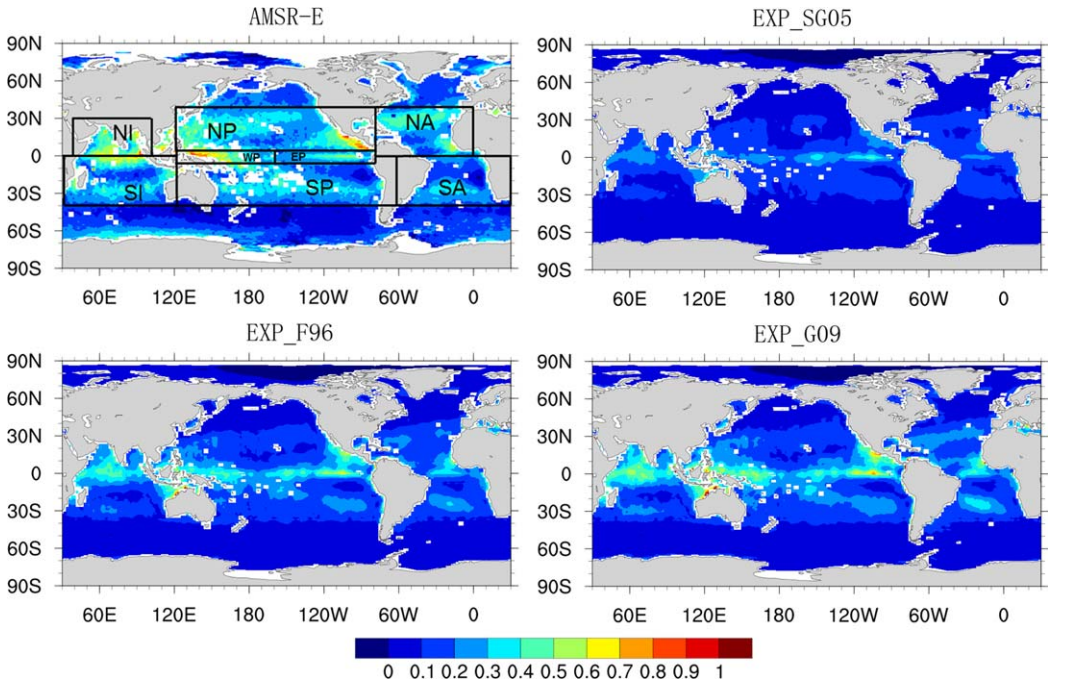

Figure 4. Annual-mean dSST from the AMSR-E SST product and from EXP_SG05, EXP_F96 and EXP_G09 during June 2002 to December 2009. The boxes are the domains where regional dSST are studied. NP: northern Pacific; SP: southern Pacific; WP: western equatorial Pacific; EP: eastern equatorial Pacific; NI: northern Indian Ocean; SI: southern Indian Ocean; NA: northern Atlantic; and SA: southern Atlantic.

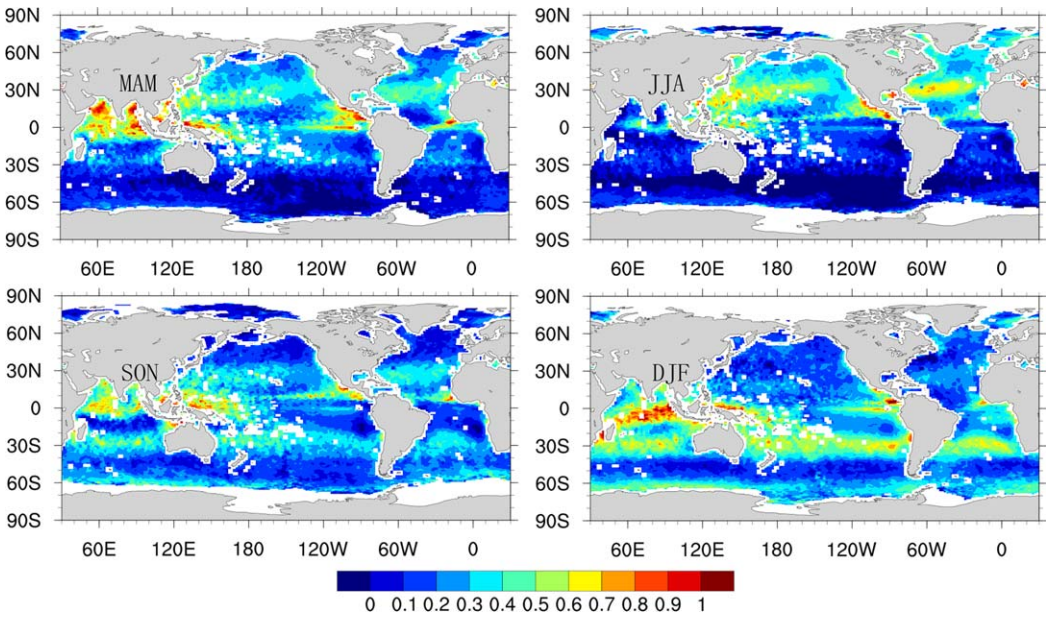

Figure 5. Seasonal distributions of dSST from AMSR-E satellite data during June 2002 to December 2009.

Despite the similarity in the distributions of dSST between satellite data and model results, the annual-mean dSST in EXP_SG05 is apparently smaller than that in the observations and the other two experiments. The peak is about 0.4°C in the eastern Pacific cold tongue and no more than 0.3°C in the other tropical areas. In EXP_F96, the annual-mean dSST in the areas with shallow sublayer depth is 0.1–0.3°C larger than that in EXP_SG05. Negligible improvements in other areas are mainly due to the lack of sublayer being formed under strong wind. The dSST in EXP_G09 is larger than that in EXP_F96 in some tropical areas. However, improvements only appear in the areas with low wind speed since dSST in EXP_G09 is larger than that in EXP_F96 only when the wind speed is less than 3.6 m/s (see supporting information Appendix A for detail).

As indicated by *Kawai and Wada* [2007], the dSST around 60°S could reach 0.3–0.5°C, especially in the boreal autumn and winter (Figure 5). However, large temperatures are not seen in our model results. This is because the net heat flux (upward) in the model is larger than SWR (downward) in these regions, leading to the absence of a sublayer, which needs to be carefully analyzed in the future.

3.2.2. Seasonality

The seasonal variation of dSST in the AMSR-E data caused by the seasonal cycle of SWR is shown in Figure 5. The dSST in most regions is the largest in summer except for the northern Indian Ocean resulting from the impact of summer monsoon. The dSST in the cold tongue area is larger in the boreal spring and winter than in the boreal summer and autumn due to wind speed change [*Clayson and Weitlich*, 2007; *Kawai and Wada*, 2007].

The seasonal-mean differences of dSST between AMSR-E data and model results in different regions (shown in Figure 4) are presented in Figure 6. Since wind speed is one of the most important factors influencing dSST, we show the differences between wind speed used to force the model and that detected by satellite radiometer in Figure 7, which can explain some of the biases in dSST.

In comparison with observations, nearly all the biases in dSST in EXP_SG05 with respect to the observations are negative, in the range of −0.37°C to −0.02°C. Nearly all the biases in EXP_SG05 are reduced in EXP_F96, by as much as 0.21°C. The RMSs of the biases are reduced as well. The improvement of the seasonal-mean biases could reach 0.28°C when using EXP_G09 instead of EXP_SG05. And all the biases are reduced to less than 0.16°C in EXP_G09, which shows good agreement with the observations.

As discussed above, when the wind speed is less than 3.6 m/s, the dSST in EXP_G09 is larger than those in EXP_F96 and in EXP_SG05. The percentage of wind speeds below 3.6 m/s can be quantified in terms of seasonality. Table 2 shows that the decreases of mean biases in the regions with large percentage of low wind

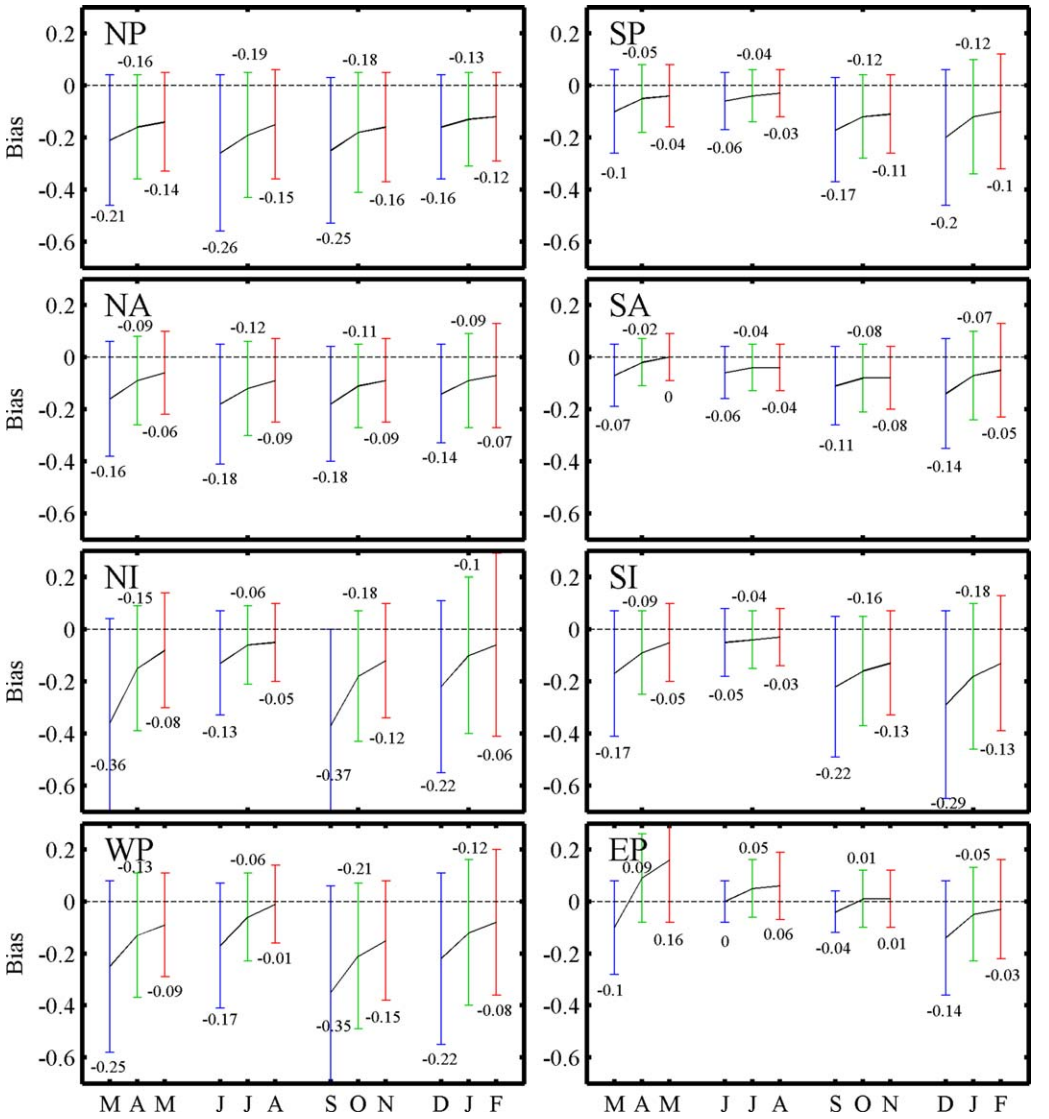

Figure 6. Mean biases of dSST between AMSR-E data and model results in different regions and seasons. The error bars represent the root mean square (RMS) of the biases in each region. Blue: EXP_SG05; green: EXP_F96; and red: EXP_G09.

speed are more significant than in the other regions in EXP_G09. The percentage of low wind speeds larger than 20% is mainly present in the Northern Pacific (NP, boreal summer), in the southern Indian Ocean (SI, boreal spring and winter), in the western equatorial Pacific (WP, boreal spring to autumn), and in the eastern equatorial Pacific (EP, boreal spring). The mean biases in these regions decrease by about 0.09–0.20°C in EXP_G09 compared to EXP_SG05. In the northern Indian Ocean (NI), the percentage could reach more than 30%, in which the biases of dSST are reduced by 0.28°C in the boreal spring and by 0.25°C in the boreal autumn.

The improvement of seasonal-mean dSST in EXP_G09 is about 0.05–0.1°C in the areas under relatively smaller percentage of low wind speed and large SWR, such as in the NP (boreal spring and autumn), in the South Pacific (SP, boreal autumn), in the North Atlantic (NA, boreal spring to autumn), in the South Atlantic (SA, boreal winter), in the NI (boreal winter), in the SI (boreal autumn), and in the WP (boreal autumn and winter). In the regions with large wind speed and weak SWR, all three experiments have mean dSST biases less than 0.1°C due to small diurnal warming in the observations and model results, such as in the SP and SA (boreal spring and summer), in the SI (boreal summer), and in the EP (boreal summer and autumn).

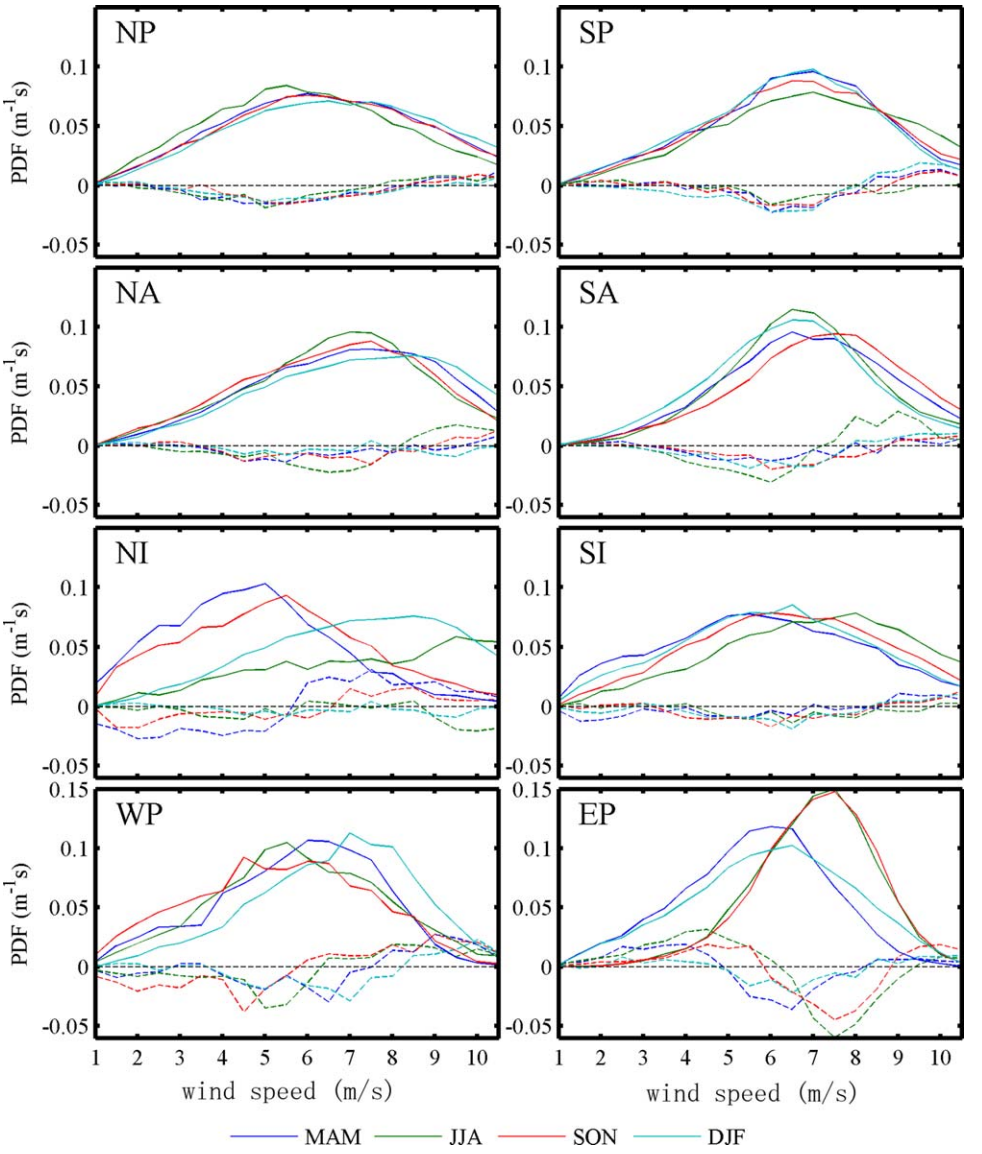

Figure 7. Probability density functions of wind speed from AMSR-E satellite data (solid lines) and the differences (dashed lines) between observations and model forcing field. Positive value means the probability in model forcing field is larger than that in the satellite data, and vice versa.

Table 2. Percentage (%) of Wind Speed Less Than 3.6 m/s in AMSR-E Data and the Differences Between Atmospheric Forcing Input and AMSR-E Data[a]

	MAM		JJA		SON		DJF	
	AMSR-E	CORE2-AMSRE	AMSR-E	CORE2-AMSRE	AMSR-E	CORE2-AMSRE	AMSR-E	CORE2-AMSRE
NP	18.3	−2.6	**23.2**	−2.8	17.5	−0.7	15.8	−1.1
SP	14.7	0.3	11.4	1.6	13.6	1.1	15.8	−2.1
NA	11.9	−0.2	13.5	−1.7	14.8	0.2	10.3	0.3
SA	9.5	0.1	7.9	−2.0	8.0	−0.1	12.9	−1.4
NI	**42.5**	−15.1	8.9	−2.4	**32.4**	−6.5	10.3	0.3
SI	**26.3**	−4.3	11.5	−0.7	17.4	−0.9	**21.8**	−1.5
WP	**21.2**	−2.3	**21.5**	−4.6	**29.6**	−9.3	11.2	0.0
EP	**21.6**	8.4	3.5	9.4	3.4	3.8	19.2	2.3

[a]The bold font means that the percentage of wind speed less than 3.6 m/s is larger than 20.0% in the satellite data, and the underline indicates the percentage of wind speed less than 3.6 m/s occurred in the atmospheric forcing input larger than that in the AMSR-E data for more than 8.0%.

Although the biases are efficiently reduced in EXP_G09, the mean biases are almost all negative due to the relatively larger wind speeds in the atmospheric forcing data than in the AMSR-E data (Figure 7), in addition to the large percentage of small dSST related to the absence of sublayer. One exception is the EP where the biases turn positive in EXP_F96 and EXP_G09 in the boreal spring. Further examining the wind speed, we find that 8.4% more of wind speed less than 3.6 m/s in the atmospheric forcing data than in the observations, while the percentage is larger at 9.4% in the boreal summer. However, the mean biases do not change much due to the large probability of strong wind during the boreal summer.

The model biases in dSST can be explained by the atmospheric forcing biases and the underestimation of dSST in EXP_SG05 and EXP_F96 under large SWR and low wind speed, as discussed earlier. It should be noted that the 6 hourly temporal resolution of the CORE2 wind speed is interpolated to each time step of the model. However, the satellite wind speed is a snapshot at its overpass time. Thus, the presence of different characteristics between the two different wind data sets is inevitable.

3.3. Comparison With Mooring Data

The intraseasonal SST variability associated with the MJO plays an important role on atmospheric fluxes, which can be successfully simulated in ocean models when the impact of diurnal variation is taken into account with high vertical resolution near the surface [*Bernie et al*., 2005, 2007; *Ling et al*., 2015]. To further evaluate the performance of different diurnal sublayer schemes, the intraseasonal SST variability and related sublayer depth are examined using skin SST and observed temperature profiles from the IMET mooring data (Figure 8).

The wind speed from the atmospheric forcing data is initially compared with that from the IMET observations. The variations of wind speed essentially agree with each other, especially during the low wind speed period. From 28 November to 8 December in 1992 and from 6 to 11 January in 1993, the wind speeds were below 4.0 m/s in both atmospheric forcing data and observations in response to the suppressed phase of the MJO. During these periods, large vertical temperature gradients occurred near the surface in the observations, which was more likely to decrease exponentially with depth as in *Gentemann et al*. [2009]. In the active phase of the MJO under large wind speed and weak SWR, the dSST values from the three experiments are all insignificant due to the sublayers rarely being formed.

Compared with dSST larger than 1°C in observations, the RMSs were 2.23, 1.79, and 1.91 in EXP_SG05, EXP_F96, and EXP_G09, respectively. The dSST in EXP_F96 agrees best with that of the observations. However, we notice that, instead of measuring directly using infrared radiometers, the skin SST from the IMET

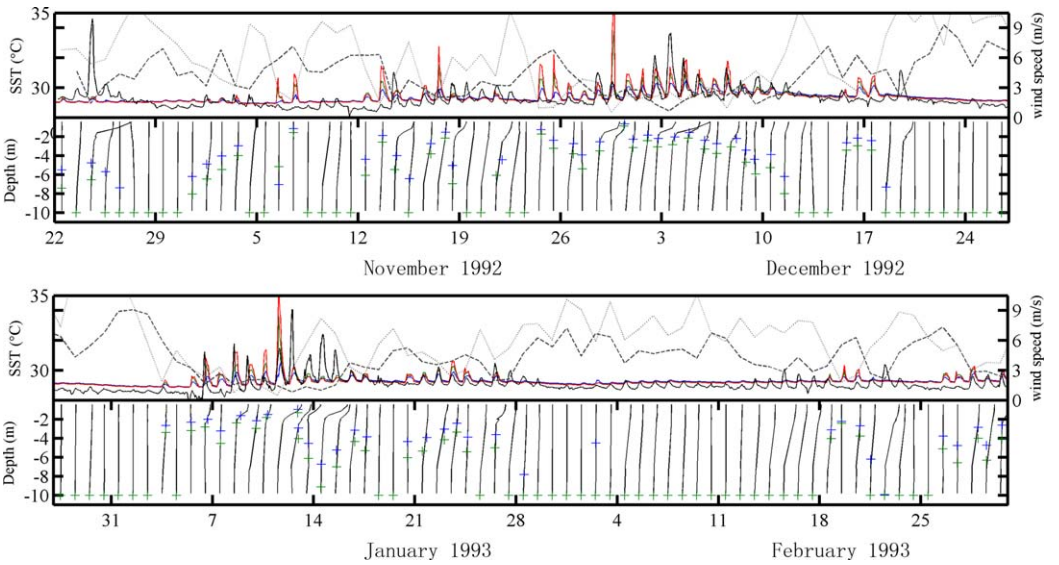

Figure 8. (top) Time series of SST and wind speed from IMET observations and model results. Solid black curve: skin SST from IMET; blue curve: SST from EXP_SG05; green curve: SST from EXP_F96; and red curve: SST from EXP_G09. Dashed black curve: wind speed from IMET at 15:00 LT; and dotted gray curve: wind speed from model atmospheric forcing data at 15:00 LT. (bottom) Temperature profiles observed by IMET at 15:00 LT. Blue crosses: sublayer depth in EXP_SG05; and green crosses: sublayer depth in EXP_F96/EXP_G09.

observations is estimated using the warm-layer model with a linearly decreased temperature profile from surface to bottom [*Fairall et al.*, 1996], which is essentially the same as the sublayer scheme used in EXP_F96. Thus, the agreement between EXP_F96 and observations is reasonable. To validate the model results more reliable and determine the most appropriate sublayer scheme in simulating intraseasonal SST during MJO, a direct observation of skin SST is required.

4. Discussion and Conclusions

The diurnal cycle of SST should be taken into account in an OGCM since it plays a significant role in air-sea interaction. The sublayer parameterization scheme following *Schiller and Godfrey* [2005] was incorporated into the three-dimensional global NEMO model to capture the diurnal cycle. Three different types of temperature profiles in the sublayer were examined to obtain the most appropriate sublayer parameterization scheme.

Comparison of the model annual-mean and seasonal distributions of dSST with the AMSR-E satellite data suggests that the sublayer scheme with exponential temperature profile performs the best to simulate large diurnal warming, significantly affecting the heat fluxes under low wind speed and strong SWR conditions. Moreover, the intraseasonal variation of SST was verified against the IMET mooring observations. The vertical temperature profiles in the observations seem to decrease exponentially under calm condition, the same as that in EXP_G09. However, the dSST in EXP_F96 agrees best with the observations, possibly due to the similar methods used in calculating the skin SST. Further validation using actual observations of skin SST is required.

In this study, the Jerlov water-type I was used for the absorption profile. However, different Jerlov water types have been examined previously in simulating diurnal variation [*Bernie et al.*, 2005; *Large and Caron*, 2015; *Schiller and Godfrey*, 2005], which could greatly influence sublayer depth and dSST due to different SWR absorption above 10 m. Thus, it is essential to evaluate the sensitivity of dSST to different Jerlov water types (supporting information Appendix B). Our results confirmed that different Jerlov water types could affect the probability distributions of dSST. Moreover, the maximum dSST could also be impacted because SWR absorption differs near the surface. The overestimation of dSST for Jerlov water type I in EXP_G09 could be reduced after changing to other Jerlov water types. However, as shown here based on Jerlov water type I, the probability of dSST larger than 2°C in EXP_G09 is about 3.8%. This percentage is quite consistent with 3.5% in the observations. The improvement using other Jerlov water types will be very limited.

Our results suggest the diurnal cycle of SST can be successfully simulated in the NEMO model at the global scale using the modified SG05 sublayer parameterization scheme with exponential temperature profile. However, the vertical temperature profile is given in advance instead of being simulated directly. If the actual temperature distribution in the vertical is the main focus, increasing the vertical resolution in the ocean model is required. After the diurnal cycle of SST is well captured, we can explore the effects of diurnal cycle on air-sea interaction using the Earth System Model framework. Moreover, the impacts on the MJO and ENSO characteristics can also be investigated in terms of mean state change of the upper ocean and atmospheric boundary layer. However, we note that the current spatial resolution of 2° may fail to simulate some localized peak warming. A higher spatial resolution experiment should be designed to obtain more accurate diurnal warming next. Finally, we note that our results are based on the NEMO with a vertical z-coordinate, which is an Eulerian-type model. The diurnal cycle in OGCMs with the arbitrary Lagrangian-Eulerian (ALE) coordinates [*Adcroft and Hallberg*, 2006; *LeClair and Madec*, 2011; *Petersen et al.*, 2015], such as Model for Prediction Across Scales-Ocean (MPAS-Ocean) [*Ringler et al.*, 2013], should be evaluated.

Acknowledgments

We acknowledge Alistair Adcroft and two anonymous reviewers for their constructive comments and suggestions for improving the manuscript. We would also like to thank Andreas Schiller for generously sharing the original code of the sublayer scheme and William Perrie for his precious suggestion in private discussion. X. Yang is supported by the National Key R&D Program of China (grant 2016YFA0602200) and the National Natural Science Foundation of China (grant 41606212). Z. Song is supported by the Basic Scientific Fund for National Public Research Institute of China (Shu-Xingbei Young Talent Program 2016S03 and the China-Korea Cooperation Project on the Trend of North-West Pacific Climate Change). Y. H. Tseng is supported by the project title "The Development and Validation of a New-generation, Fully-Coupled Global Climate System Model" (grant 106–2111-M-002–001). F. Qiao is supported by the National Natural Science Foundation of China-Shandong Joint Fund for Marine Science Research Centers (grant U1606405). Q. Shu is supported by the National Programme on Global Change and Air-Sea Interaction (grant GASI-IPOVAI-06). All the simulations of this work were carried out at the National Supercomputer Center in Changsha on its Tianhe-1 through PARATERA's service. The in situ data used in this study are available from the Woods Hole Oceanographic Institution (http://www.whoi.edu/). The AMSR-E data used in this paper are produced by the Remote Sensing Systems (ftp://ftp.nodc.noaa.gov/pub/data.nodc/ghrsst/).

References

Adcroft, A., and R. Hallberg (2006), On methods for solving the oceanic equations of motion in generalized vertical coordinates, *Ocean Modell.*, *11*(1–2), 224–233.

Antonov, J. I., D. Seidov, T. P. Boyer, R. A. Locarnini, A. V. Mishonov, H. E. Garcia, O. K. Baranova, M. M. Zweng, and D. R. Johnson (2010), World Ocean Atlas 2009, in *Volume 2: Salinity, NOAA Atlas NESDIS 68*, edited by S. Levitus, 184 pp., U.S. Gov. Print. Off., Washington, D. C.

Bernie, D. J., S. J. Woolnough, J. M. Slingo, and E. Guilyardi (2005), Modeling diurnal and intraseasonal variability of the ocean mixed layer, *J. Clim.*, *18*(8), 1190–1202.

Bernie, D. J., E. Guilyardi, G. Madec, J. M. Slingo, and S. J. Woolnough (2007), Impact of resolving the diurnal cycle in an ocean–atmosphere GCM. Part 1: A diurnally forced OGCM, *Clim. Dyn.*, *29*(6), 575–590.

Bernie, D. J., E. Guilyardi, G. Madec, J. M. Slingo, S. J. Woolnough, and J. Cole (2008), Impact of resolving the diurnal cycle in an ocean-atmosphere GCM. Part 2: A diurnally coupled CGCM, *Clim. Dyn.*, *31*(7–8), 909–925.

Clayson, C. A., and D. Weitlich (2007), Variability of tropical diurnal sea surface temperature*, *J. Clim.*, *20*(2), 334–352.

Danabasoglu, G., W. G. Large, J. J. Tribbia, P. R. Gent, B. P. Briegleb, and J. C. McWilliams (2006), Diurnal coupling in the tropical oceans of CCSM3, *J. Clim.*, *19*(11), 2347–2365.

Fairall, C. W., E. F. Bradley, J. S. Godfrey, G. A. Wick, J. B. Edson, and G. S. Young (1996), Cool-skin and warm-layer effects on sea surface temperature, *J. Geophys. Res.*, *101*(C1), 1295–1308.

Filipiak, M. J., C. J. Merchant, H. Kettle, P. Le Borgne, M. J. Filipiak, C. J. Merchant, H. Kettle, and P. Le Borgne (2012), An empirical model for the statistics of sea surface diurnal warming, *Ocean. Sci.*, *8*(2), 197–209.

Flato, G., et al. (2013), Evaluation of climate models, in *Climate Change 2013: The Physical Science Basis. Contribution of Working Group I to the Fifth Assessment Report of the Intergovernmental Panel on Climate Change*, edited by T. F. Stocker et al., Cambridge Univ. Press, Cambridge, U. K.

Gentemann, C. L., P. J. Minnett, and B. Ward (2009), Profiles of ocean surface heating (POSH): A new model of upper ocean diurnal warming, *J. Geophys. Res.*, *114*, C07017, doi:10.1029/2008JC004825.

Griffies, S. M., A. Biastoch, C. Böning, F. Bryan, G. Danabasoglu, E. P. Chassignet, M. H. England, R. Gerdes, H. Haak, and R. W. Hallberg (2009), Coordinated Ocean-ice Reference Experiments (COREs), *Ocean Modell*, *26*(1), 1–46.

Ham, Y., J. Kug, I. Kang, F. Jin, and A. Timmermann (2010), Impact of diurnal atmosphere–ocean coupling on tropical climate simulations using a coupled GCM, *Clim. Dyn.*, *34*(6), 905–917.

Jerlov, N. G. (1976), *Marine Optics*, 231 pp., Elsevier, New York.

Kawai, Y., and A. Wada (2007), Diurnal sea surface temperature variation and its impact on the atmosphere and ocean: A review, *J. Oceanogr.*, *63*(5), 721–744.

Large, W. G., and J. M. Caron (2015), Diurnal cycling of sea surface temperature, salinity, and current in the CESM coupled climate model, *J. Geophys. Res. Oceans*, *120*, 3711–3729, doi:10.1002/2014JC010691.

Large, W. G., and S. G. Yeager (2004), Diurnal to decadal global forcing for ocean and sea-ice models: The data sets and flux climatologies, NCAR Technical Note NCAR/TN-460+STR, doi:10.5065/D6KK98Q6.

Large, W. G., and S. G. Yeager (2009), The global climatology of an interannually varying air–sea flux data set, *Clim. Dyn.*, *33*(2–3), 341–364.

Leclair, M., and G. Madec (2011). $\tilde{Z}$ -Coordinate, an arbitrary Lagrangian–Eulerian coordinate separating high and low frequency motions, *Ocean Modell.*, *37*(3–4), 139–152.

Ling, T., M. Xu, X.-Z. Liang, J. X. L. Wang, and Y. Noh (2015), A multilevel ocean mixed layer model resolving the diurnal cycle: Development and validation, *J. Adv. Model. Earth Syst.*, *7*, 1680–1692, doi:10.1002/2015MS000476.

Locarnini, R. A., A. V. Mishonov, J. I. Antonov, T. P. Boyer, H. E. Garcia, O. K. Baranova, M. M. Zweng, and D. R. Johnson (2010), World Ocean Atlas 2009, in *Volume 1: Temperature, NOAA Atlas NESDIS 68*, edited by S. Levitus, 184 pp., U.S. Gov. Print. Off., Washington, D. C.

Madec, G. (2008), NEMO ocean engine, in *Note du Pole de Modelisation*, Inst. Pierre-Simon Laplace, France.

Masson, S., P. Terray, G. Madec, J. Luo, T. Yamagata, and K. Takahashi (2012), Impact of intra-daily SST variability on ENSO characteristics in a coupled model, *Clim. Dyn.*, *39*(3–4), 681–707.

Petersen, M. R., D. W. Jacobsen, T. D. Ringler, M. W. Hecht, and M. E. Maltrud (2015), Evaluation of the arbitrary Lagrangian–Eulerian vertical coordinate method in the MPAS-ocean model, *Ocean Modell.*, *86*, 93–113.

Ringler, T., M. Petersen, R. L. Higdon, D. Jacobsen, P. W. Jones, and M. Maltrud (2013), A multi-resolution approach to global ocean modeling, *Ocean Modell.*, *69*(C), 211–232, doi:10.1016/j.ocemod.2013.04.010.

Schiller, A., and J. S. Godfrey (2005), A diagnostic model of the diurnal cycle of sea surface temperature for use in coupled ocean-atmosphere models, *J. Geophys. Res.*, *110*, C11014, doi:10.1029/2005JC002975.

Soloviev, A., and R. Lukas (1997), Observation of large diurnal warming events in the near-surface layer of the western equatorial Pacific warm pool, *Deep Sea Res., Part I*, *44*(6), 1055–1076.

Steele, M., R. Morley, and W. Ermold (2001), PHC: A global ocean hydrography with a high quality Arctic Ocean, *J. Clim.*, *14*, 2079–2087.

Webster, P. J., et al. (1996), Clouds, radiation, and the diurnal cycle of sea surface temperature in the tropical western Pacific, *J. Clim.*, *9*(8), 1712–1730.

Weihs, R. R., and M. A. Bourassa (2014), Modeled diurnally varying sea surface temperatures and their influence on surface heat fluxes, *J. Geophys. Res. Oceans*, *119*, 4101–4123, doi:10.1002/2013JC009489.

Zeng, X., and A. Beljaars (2005), A prognostic scheme of sea surface skin temperature for modeling and data assimilation, *Geophys. Res. Lett.*, *32*, L14605, doi:10.1029/2005GL023030.